Check for updates

Metal–organic framework MIL-101(Fe) functionalized with folic acid as a multifunctional nanocarrier for targeted chemotherapy– photodynamic therapy†

Eman Serag,[a,b] Esmail M. El-Fakharany, [ID][c,d,e] Sherif F. Hammad[f] and Mohamed E. El-Khouly [ID] *[a]

A novel folic acid-conjugated, iron-based MOF (MIL-101(Fe)) loaded with 1,8-acridinediones (DO8) was developed for targeted photodynamic therapy (PDT) of HepG-2 cells. This composite aims to trigger an anticancer response through sequential PDT and chemotherapy. The nanocomposite exhibited high stability in a physiological environment with a pH of 7.4. It was also able to release DO8 continuously in an acidic environment with a pH of 5, which shows that it can adapt to the conditions in the tumor microenvironment. The MIL-101(Fe)MOF-FA@DO8 nanoparticles (NPs) with 30% and 50% DO8 have been studied *in vitro* under different conditions (light and dark) and have been shown to be compatible with living tissues and specifically target HepG-2 cells. The IC_{50} values of 50% DO8 and 30% DO8 loaded MOF-FA were found to be 88.67 and 105.9 µg mL^{-1} under dark conditions, respectively. Under light conditions, they demonstrated the highest efficacy in inhibiting tumor cell growth. The IC_{50} values were found to be 8.94 and 11.78 µg mL^{-1}. Flow cytometry analysis of annexin V/PI-stained apoptotic and necrotic cells in HepG-2 cells treated with the modified MIL-101-FA@50% DO8 NPs at IC_{50} doses under both dark and light conditions indicates that the primary mechanism of cell death is necrosis, likely due to the enhanced formation of reactive oxygen species (ROS) under light conditions compared to that under dark conditions. This increased reactive oxygen species (ROS) generation leads to extensive membrane rupture, resulting in significant cell damage after treatment with the modified MIL-101-FA@50% DO8 NPs. These findings underscore the potential of this nanocomposite as an effective PDT agent for targeted cancer therapy.

Introduction

Photodynamic therapy (PDT) is a promising approach for the treatment of cancer and bacterial infections.[1] The therapeutic effect of this process is achieved by utilizing reactive oxygen species (ROS) that are produced by photosensitizers (PSs) when exposed to specific light and in the presence of oxygen (O_2).[2] Photodynamic therapy (PDT) enables accurate treatments by controlling the size of the illuminated region. The low or minimally invasive nature, limited side effects, and high selectivity of this approach have garnered considerable attention in cancer therapy.[3] However, it is important to note that most PSs do not exclusively accumulate solely in the targeted lesions.[4] Furthermore, these substances can also accumulate on the surface of the skin and healthy tissues, leading to indiscriminate phototoxic harm. Recently, metal–organic frameworks (MOFs) have been suggested for various purposes, including selective gas adsorption and separation, gas storage, optical devices, sensors, catalysis, drug delivery systems, and biomedicine.[5] This is due to their high porosity and uniform pores, which allow for the effective trapping of large quantities of drugs.

However, the specific crystalline network of MOFs has the ability to not only allow molecules to enter the pores but also

[a]*Nanoscience Program, Institute of Basic and Applied Science, Egypt-Japan University of Science and Technology (E-JUST), New Borg El-Arab City, Alexandria, Egypt. E-mail: mohamed.elkhouly@ejust.edu.eg*

[b]*Marine Pollution Department, Environmental Division, National Institute of Oceanography and Fisheries, Kayet Bey, Elanfoushy, Alexandria, Egypt*

[c]*Protein Research Department, Genetic Engineering and Biotechnology Research Institute (GEBRI), City of Scientific Research and Technological Applications (SRTA-City), New Borg El-Arab, Alexandria 21934, Egypt*

[d]*Pharmaceutical and Fermentation Industries Development Centre (PFIDC), City of Scientific Research and Technological Applications (SRTA-City), New Borg El-Arab, Alexandria, Egypt*

[e]*Pharos University in Alexandria; Canal El Mahmoudia Street, Beside Green Plaza Complex 21648, Alexandria, Egypt*

[f]*PharmD program, Egypt-Japan University of Science and Technology (E-JUST), New Borg El-Arab City, Alexandria, Egypt*

†Electronic supplementary information (ESI) available. See DOI: https://doi.org/10.1039/d4bm01738b

to coordinate the molecules of interest with metals and arrange them in specific positions as part of the structure.[6] Undoubtedly, the inclusion of a metal introduces a wide range of possibilities for combining inorganic and organic components, resulting in materials where both the metal and the molecule play important roles, leading to numerous applications.[7] Extensive research has been conducted on the metal's role as a co-adjuvant in PDT. Its functions include reducing hypoxia, decreasing antioxidant species, generating ROS, and serving as a contrast agent for imaging-guided therapy.[8] Iron is a metal that has been studied in PS-based MOFs for PDT theranostic systems.[9] These systems have the ability to both diagnose and treat, using magnetic resonance imaging (MRI) for diagnosis and Fenton reactions to combat hypoxia in PDT.[10] Currently, various methods have been used to enhance the amount of oxygen at the tumor location. These include delivering oxygen-rich substances to the tumor site using nanocarriers.[11] The concentration of hydrogen peroxide (H_2O_2) is greater (100 μM–1 mM) in tumour cells compared to that in normal cells.[12] Thus, the process of decomposing H_2O_2 within tumor cells to generate oxygen emerges as a highly promising strategy for enhancing the oxygen levels within cancer cells. The decomposition methods of H_2O_2 typically involve the use of catalase and the Fenton reaction with oxygen.[13] Previously, a Fe-MOF catalyst was used to facilitate the decomposition of H_2O_2 by DOX and MV-PAH, resulting in the production of a combination of reactive oxygen species (ROS) and chemotherapy.[14] This approach was employed to enhance the anti-cancer efficacy.

In another approach, zinc-phthalocyanine (ZnP) photosensitizers inserted into the pores of a nanoscale metal–organic framework called Hf12-QC (QC = 2″,3′-dinitro-[1,1′:4′,1″;4″,1‴-quaterphenyl]-4,4‴-dicarboxylate).[15,16] ZnP@Hf-QC-mediated photodynamic therapy (PDT) demonstrated remarkable effectiveness in inhibiting tumor growth, with over 99% inhibition and 80% cure rates observed in two murine colon cancer models.[16] Zeolitic imidazolate framework-8 (ZIF-8) nanoparticles were employed to simultaneously encapsulate chlorin e6 (Ce6), a powerful photosensitizer, and cytochrome c (Cyt c), a protein that induces apoptosis. Subsequently, the nanoparticle was coated with a hyaluronic acid (HA) shell to create a targeted nanoplatform (Ce6/Cyt c@ZIF-8/HA) with activity against cancer cells.[17] The *in vitro* and *in vivo* experiments demonstrate the ability of Ce6/Cyt c@ZIF-8/HA to target cancer cells and undergo pH-responsive decomposition and release.

Among the photosensitizers for PDT, the heterocyclic acridinediones were found to be efficient photosensitizers for therapeutic treatments for several clinical conditions through the binding to DNA and efficiently inhibiting the proliferation of cancer cells. Recently, our group successfully synthesized an *N*-substituted acridine-1,8-dione derivative (DO8), which is a derivative resulting from the addition of a phthalimide group to the acridinedione backbone. The studies of DO8 showed its unique photochemical properties, which render it as a potential chemotherapeutic agent. Along this line, we report herein the utilization of DO8 for fabricating novel nanoplatforms for photodynamic applications. The DO8 compound was enclosed within the MIL-101(Fe)MOF material and then coupled with the cancer-specific ligand folic acid in order to specifically target cancer cells in deep tissue. Due to the presence of an excessive amount of folate receptors (FRs) on the surface of cancer cells and the existence of folic acid in the fabricated MIL-101(Fe)MOF-FA@DO8 nanoplatform, the DO8 compound can be directed towards the cancer cells. The MIL-101(Fe)MOF NPs exhibit characteristic behavior in an oxygen-depleted setting and maintain their capacity to act as a peroxidase/catalase, enabling the breakdown of H_2O_2 and the generation of O_2. This feature allows it to mitigate the hypoxia induced by PDT and enhance the efficacy of PDT.

Materials and methods

Materials

The following chemicals were purchased from Sigma-Aldrich Dresden Germany: iron chloride hexahydrate ($FeCl_3·6H_2O$), terephthalic acid (H_2BDC), dimethylformamide (DMF), and ethanol. Additionally, dimethyl sulfoxide (DMSO, 99.8%), phosphate buffered saline (PBS, 99%), 1-(3-dimethylaminopropyl)-3-ethylcarbodiimide hydrochloride (EDC, 99.8%), and *N*-hydroxysuccinimide (NHS, 99%) were purchased from Merck Co. Folic acid (FOLA, 97% Aldrich) was also obtained from Sigma-Aldrich. Dulbecco's Phosphate-Buffered Saline (DPBS), DMEM, and Triton X-100 were sourced from Sigma Aldrich (USA). Human cell lines, including lung fibroblast (Wi-38), breast carcinoma (MDA), hepatoma (HepG-2), and lung carcinoma (A549), were obtained from the American Type Culture Collection (ATCC), Manassas, Virginia, USA. Fetal bovine serum and a sterile penicillin/streptomycin solution for cell culture were acquired from BioWest, France. The Apoptosis/Necrosis Detection Kit (BD Pharmingen™ FITC Annexin V Apoptosis Detection Kit I) was supplied by BD Biosciences, Germany. All experiments were conducted using ultrapure water. The *in vitro* study was conducted at the Protein Research Department of the Genetic Engineering and Biotechnology Research Institute (GEBRI) in the City of Scientific Research and Technological Applications (SRTA City), found in New Borg Al-Arab City, Alexandria, Egypt.

Methods

Preparation of MIL-101(Fe)MOF nanoparticles. MIL-101(Fe) MOF NPs were synthesized and developed based on literature reports.[18] Concisely, a total of 2.48 mmol of $FeCl_3·6H_2O$ and 1.24 mmol of terephthalic acid were introduced into 20 mL of DMF. The resulting mixture was agitated using a magnetic stirrer. Subsequently, the uniform and fully dissolved solution was subjected to heating at a temperature of 110 °C for a duration of 20 hours in a Teflon reactor. Subsequently, the initial product underwent centrifugation at a speed of 13 000 (rpm). The synthesized MOF was purified by washing it with methanol several times. The light orange product that had been cleaned was dried overnight in a vacuum oven at 70 °C.

Activated folic acid functionalized MIL-101(Fe)MOF nanoparticles. Prior to conjugating folic acid with MIL-101(Fe) MOF NPs, it is crucial to activate the carboxylate group of folic acid to synthesize the *N*-hydroxysuccinimide (NHS) ester of folic acid (activated FOLA). Folic acid is composed of two carboxyl groups, referred to as α and γ. The γ-carboxyl group exhibits significantly higher reactivity in carbodiimide-mediated coupling.[19] As a result, folic acid is chemically linked to MIL-101(Fe)MOF NPs by activating the γ-COOH group of folic acid using coupling agents, 1-(3-dimethylaminopropyl)-3-ethylcarbodiimide hydrochloride (EDC) and *N*-hydroxysuccinimide (NHS). The folic acid was activated by dissolving 0.32 g of folic acid in 20 mL of phosphate buffer with a pH of 7. The resulting mixture was then sonicated for one hour. The carboxylate group of folic acid was activated by adding 0.30 g of NHS and 0.15 g of EDC. The mixture was then agitated overnight in the dark. Subsequently, the material was subjected to drying in a vacuum oven at a temperature of 60 °C for 12 h.[20] To functionalize MIL-101(Fe)MOF NPs, MIL-101(Fe)MOF NPs were combined with activated FA at a ratio of 2 : 1. The mixture was reacted in 30 mL of DMF with vigorous stirring for 72 hours. Subsequently, the mixture underwent precipitation through centrifugation at a speed of 9000 rpm for 20 minutes. Subsequently, the samples underwent two rounds of rinsing using a methanol–water mixture with a ratio of 1 : 1 to remove any remaining excess targeting ligands. Afterwards, the MIL-101(Fe)MOF-FA NP sample was immersed in a 30 mL *n*-hexane solution for a period of 4 hours in order to facilitate the exchange of solvents. Subsequently, the samples underwent vacuum drying at a temperature of 60 °C for a duration of 12 hours (Scheme 1).[21]

### Assessment of photosensitizer loading and *in vitro* release

A DO8 photosensitizer, derived from the acridine-1,8-dione family, was synthesized as previously described.[22] Its structural characterization was confirmed by ^{1}H NMR, FTIR, and LC-MS (see the ESI†). DO8 was incorporated into MIL-101(Fe)MOF-FA NPs *via* wet impregnation (Scheme 1). Specifically, 30 and 50 wt% of DO8 were dissolved in 20 mL of DMSO using sonication for 10 minutes at 25 °C. Subsequently, 0.1 g of MIL-101(Fe)MOF-FA was added to the solution, and the mixture was stirred at 350 rpm for 24 hours at 25 °C. After centrifugation, the MIL-101(Fe)MOF-FA@DO8 NP composite was isolated. The supernatant was analyzed to determine the encapsulation efficiency (EE (%)) of DO8 in the MOF.[23,24]

$$\text{Encapsulation efficiency} \, (\%) = \frac{\text{drug}_{\text{total}} - \text{drug}_{\text{unloaded}}}{\text{drug}_{\text{total}}} \times 100$$

(1)

The term "drug$_{\text{total}}$" refers to the initial weight of the photosensitizer PS before it is loaded onto the carrier. On the other hand, "drug$_{\text{unloaded}}$" refers to the weight of the free PS in the supernatant.

Characterization

The morphology of the synthesized MIL-101(Fe)MOF NPs was examined using a scanning electron microscope (SEM JEOL JSM 6360LA, Japan). Infrared (IR) spectra were recorded using a
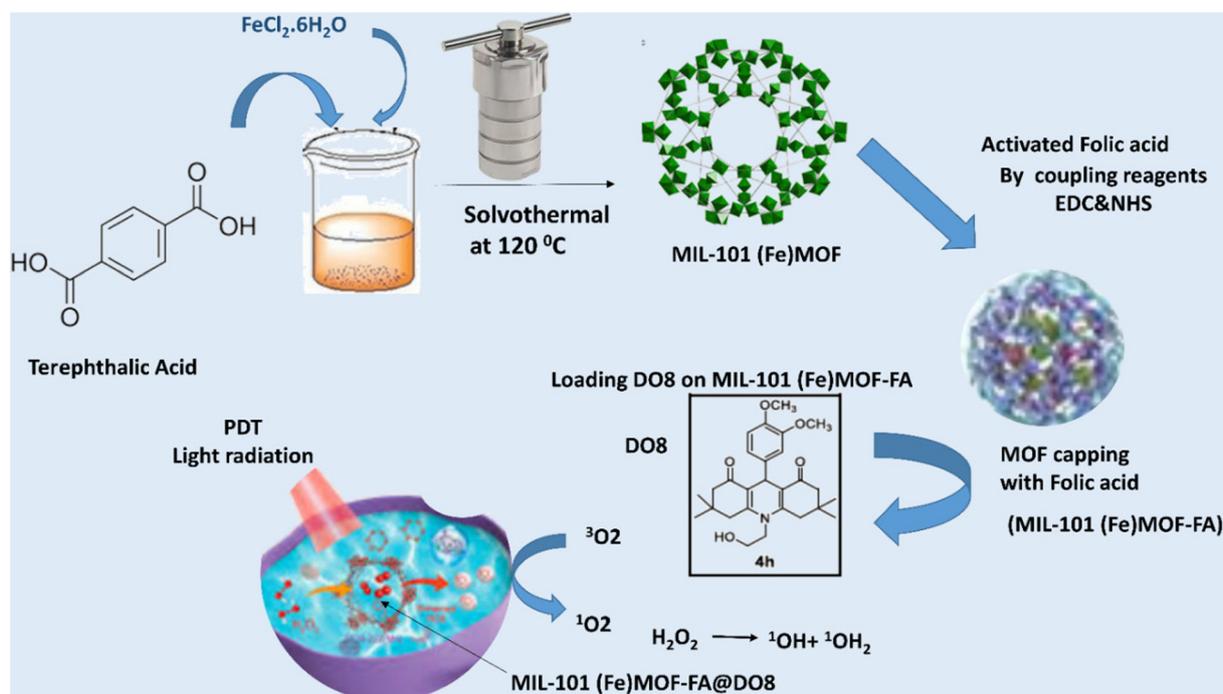
Scheme 1 Illustration of the design of loading DO8 as a new photosensitizer on MIL-101(Fe)MOF conjugated folic acid.

Bruker Alpha IR (100 FT-IR) spectrophotometer. The specific Langmuir and BET surface area, pore size, and pore volume can be determined by analyzing the N_2 adsorption/desorption isotherms. The measurement of nitrogen isotherms was conducted at a temperature of 77 K using a BELSORP-miniX instrument. The instrument was supplied with commercial software version 1.0.9.0, which was used for the calculation and analysis of the data. UV-VIS-NIR spectrophotometric (Shimadzu, model UV-2600) and spectrofluorometric (Shimadzu, model RF-6000) techniques were used to measure the optical absorption and fluorescence spectra of MIL-101(Fe)MOF NPs, MIL-101(Fe) MOF-FA NPs, and MIL-101(Fe)MOF-FA@DO8 NPs, respectively. An X-ray 7000, Shimadzu, Japan, was used to acquire X-ray diffraction images of the samples. Measurements of the Bragg angle (2θ) were within the range of 10 to 80 degrees. The X-ray source consists of a copper target that is scanned at a rate of 4 degrees per minute. The source operates at a voltage of 30 kilovolts (kV) and a current of 30 milliamperes (mA). The zeta potential and DLS of the samples were conducted by Malvern Instruments using a Nano-ZS (Malvern Instruments, UK) at 25 °C and pH 7. The intensity emission spectrum of singlet oxygen, generated by DO8 and MIL-101 MOF-FA@DO8 NPs, was measured using the time-correlated single photon counting (TCSPC) technique. The measurements were performed with a FluoTime 300 instrument from PicoQuant, Germany, which was equipped with a near-infrared photomultiplier tube (NIR-PMT) detector. The spectral range of the detector was set to 950–1400 nm. The LDH-P-C-640B laser head was employed as an excitation source for generating picosecond pulses.

Determination of singlet oxygen quantum yields

Singlet oxygen quantum yields are detected directly by measurement of singlet oxygen phosphorescence ($\lambda_{em} \sim 1275$ nm) following photoexcitation of the examined compounds at ambient temperature in acetonitrile. The compounds are excited using the third harmonic of a Q-S Nd:YAG laser ($\lambda = 355$ nm, ~ 8 ns pulse length, and pulse energy ≤ 20 mL). The specific laser model used is LP980 from an Edinburgh Instruments laser flash photolysis system. The luminescent signal of singlet oxygen ($^1O_2$) at a wavelength of 1275 nm was measured using a Hamamatsu H10330-45 near-infrared (NIR) detector. The optical densities of the substance under study and the standard were equated at a wavelength of 355 nm.[25,26]

Extracellular ˙OH detection (methylene blue degradation by ˙OH)

A total of 1 mg of MIL-101(Fe)MOF-FA@DO8 NPs was dispersed in 5.0 mL of methylene blue (MB) solution containing 20 mM hydrogen peroxide H_2O_2. The solution was bombarded with LED light at 400 nm and 1.5 W cm^{-2} for different time intervals. Following irradiation, the MB solution was centrifuged to remove MIL-101(Fe)MOF-FA@DO8 NPs, and the absorbance at 664 nm was measured with a UV-vis spectrophotometer. For comparison, a similar experiment was carried out in the absence of light or H_2O_2 to examine MB deterioration under those conditions.[27]

Stability examinations of the synthesized MIL-101(Fe) MOF@DO8 NPs

The stability of MIL-101(Fe)MOF@DO8 NPs was examined using UV-vis spectroscopy and FTIR methods. A 1 mg mL^{-1} aliquot of the colloidal solution of MIL-101(Fe)MOF@DO8 was dissolved in PBS and monitored for 1–21 days.[28]

In vitro release kinetic analysis

The release experiments of DO8 from MIL-101(Fe)MOF-FA@DO8 NPs were conducted using the dialysis bag method at pH 5 and pH 7.4. For the typical experiment, 1 mg mL^{-1} aliquots of MIL-101(Fe)MOF-FA@DO8 NPs were placed in dialysis bags (Sigma Aldrich) with a molecular weight cut-off of 3000 Da and a cellulose membrane with an average flat width of 33 mm. These bags were then incubated in 50 mL of an external medium. The system was consistently and gently stirred at a temperature of 37 °C. At regular time intervals, ranging up to 72 hours, 1 mL samples were taken from the external medium to measure the amount of photosensitizer using spectroscopy. Following the measurement, each aliquot was returned to the receiver vessel to ensure a consistent volume. A study was undertaken to plot the release profile of a drug with time, showing the percentage of drugs released. In order to investigate the release mechanism of DO8 from MIL-101(Fe)MOF-FA@DO8 NPs, the data were analyzed using various models, including zero order, first order, the Korsmeyer and Peppas model, and Higuchi's diffusion control model. The equations used for each model are as follows:[29,30]

Zero-order equation:

$$Q_t = Q_0 + K_0 t \tag{2}$$

Q_t represents the amount of dose dissolved at a specific time t, Q_0 represents the initial dose at the beginning of the experiment, and K_0 represents the zero-order release constant, which is stated as a concentration per unit time.

First-order equation:

$$\text{Log } Q_t = \log Q_0 - Kt/2.303 \tag{3}$$

Q_0 is the initial drug concentration, while K is a first-order constant.

Korsmeyer and Peppas model:

$$M_T/M_\infty = Kt^n \tag{4}$$

$$\text{Log } (M_T/M_\infty) = \log k + n \log t \tag{5}$$

M_T and M_∞ represent the proportions of the drug that have been released at time t and at infinite time, respectively. The kinetic constant k and the release exponent n are used to describe the rate and mechanism of drug transport.

Higuchi's diffusion control model:

$$Q = K_H t^{1/2} \tag{6}$$

The variable Q represents the total amount of drugs released at a specific time, denoted as "t". The constant K_H refers to the Higuchi constant, while "t" represents the time in hours.

Evaluating the biological activities of the synthesized ligands

In vitro cytotoxicity assay. The cytotoxicity of the synthesized compounds in different quantities, MIL-101(Fe)MOF-FA@50% DO8 NPs, MIL-101(Fe)MOF-FA@30% DO8 NPs, MIL-101(Fe) MOF-MOF NPs, MIL-101(Fe)MOF-FA NPs, and DO8, was evaluated against the Wi-38, MDA, HepG-2, and A549 cell lines under both dark and light conditions using the Thiazolyl Blue Tetrazolium Bromide (MTT) method.[23,31] Concisely, 96-well plates containing 10×10^3 cells of the Wi-38, MDA, HepG-2, and A549 cell lines were exposed to overnight incubation at 37 °C, 5% CO_2, and 90% humidity. Each well containing the synthesized compounds was supplemented with a total volume of 200 μL of DMEM for Wi-38, MDA, and A549 cells and RPMI-1640 media for HepG-2 cells. The final concentrations of the compounds were 25, 50, 100, 200, 400, and 800 μg mL^{-1}. This was done under dark conditions. Nevertheless, all cells were subjected to synthesized compounds at concentrations of 1.5, 3.0, 6.0, 12.0, 24.0, and 48.0 μg mL^{-1} in the presence of laser irradiation at 400 nm and 1.5 W cm^{-2} for 10 min. Following a 48 hour incubation period at a temperature of 37 °C and with a 5% concentration of CO_2, the cells underwent three BPS washes to eliminate any debris and non-viable cells. Following the removal of media and three washes with PBS, 200 μL of MTT solution (0.5 mg mL^{-1}) was introduced into each well. Subsequently, the mixture underwent vigorous agitation for a duration of five minutes at a speed of 150 rpm, while the plates were positioned in an incubator containing 5% carbon dioxide (CO_2) for a period of 2–4 hours. This facilitated the metabolic activity of the living cells to process the MTT. Subsequently, the MTT solution was substituted with 200 μL of dimethyl sulfoxide (DMSO) in each well and agitated for 5 minutes at a speed of IC_{50} revolutions per minute.

The optical density of the formazan crystals that were formed, which indicates that the cell viability in each well was measured at a wavelength of 570 nm. The percentage of cell viability in each well was determined by applying the following formula: the relative cell viability = $[X/Y] \times 100$, where X is the mean optical density of the tested sample and Y is the mean optical density of the reference (control) sample. X represents the average optical density of the tested sample. The IC_{50} values were determined by analyzing the concentrations using GraphPad Prism version 8.0 software. The selectivity index (SI) values were calculated by dividing the average IC_{50} values of normal cells by the average IC_{50} values of cancer cell lines. Therefore, the calculated SI values appear to accurately represent the *in vivo* anticancer effect. The samples underwent triplicate testing and were compared to untreated cells as a negative reference.

The influence of the synthetic compounds on the formation of reactive oxygen species (ROS)

Based on the obtained results of the MTT assay, the level of reactive oxygen species (ROS) in HepG-2 cells was measured under both dark and light conditions using 2′,7′-dichlorodihy-drofluorescein diacetate (DCFH-DA).[32] Following 48 hour treatment of HepG-2 cells with the synthesized compounds, the levels of intracellular ROS were measured in both untreated and treated cells. Fluorescence microscopy analysis was conducted to capture the images of cells and investigate the generation of reactive oxygen species (ROS).

Assessment of the mode of cell death using flow cytometry

Based on the obtained results of the MTT assay, HepG-2 cells were treated with MIL-101-FA@50% DO8 NPs under both dark and light conditions (irradiation time 10 min). The treated cells were collected and stained with Annexin V FITC and PI. The annexin-stained apoptotic population of the stained cells was measured at an FITC signal detector (Annexin V-FITC) against the PI-stained necrotic emission signal detector (PI) for cells. The data were then analyzed using FCS Express (De Novo software).

Statistical analysis

The experiments were conducted in triplicate ($n = 3$), and the data are presented as the mean ± standard deviation. Data are being analyzed using the Origin Pro software and the GraphPad Prism Software version 7. The statistical significance between the groups was assessed using one-way analysis of variance (ANOVA). Statistical significance was determined for differences between the groups with $p < 0.05$.

Results and discussion

Preparation of a DO8 photosensitizer and its characterization

Our previous study established the synthesis of new heterocyclic derivatives, notably acridine-1,8-dione derivatives. The synthesis was carried out using the Hantzsch method, as illustrated in Scheme S1.† The execution of this process was straightforward, and the production of the desired products was abundant. The characterization of the synthesized DO8 (HNMR, ^{13}C, and LC-Mass) is illustrated in ESI Fig. S1 and S2.†

Synthesis and characterization of ML 101(Fe)MOF NPs

Due to their exceptional stability, MIL-101(Fe)MOF NPs, a well-known metal–organic framework (MOF), have previously served as a carrier for bioactive substances.[32] MIL-101(Fe)MOF NPs exhibit a rigid zeotype crystal structure known as MTN, which consists of two distinct types of cages. The cavities are medium-sized, with a diameter of 2.9 nm.[26] Pentagonal windows with an opening of 1.2 nm can access these cavities.[33] Additionally, there are larger cavities with a diameter of 3.4 nm that exhibit hexagonal windows measuring 1.6 nm in diameter.[30] The expansive MOF cavities, along with their comparatively large openings, allow for the inclusion of bulky pharmacological molecules. The morphology of the synthesized MIL-101(Fe)MOF NPs was examined using a scanning electron microscope, as depicted in Fig. 1A. The image reveals an octahedral structure with a smooth surface, and the MIL-101(Fe)MOF NPs have a size ranging from 400 nm to
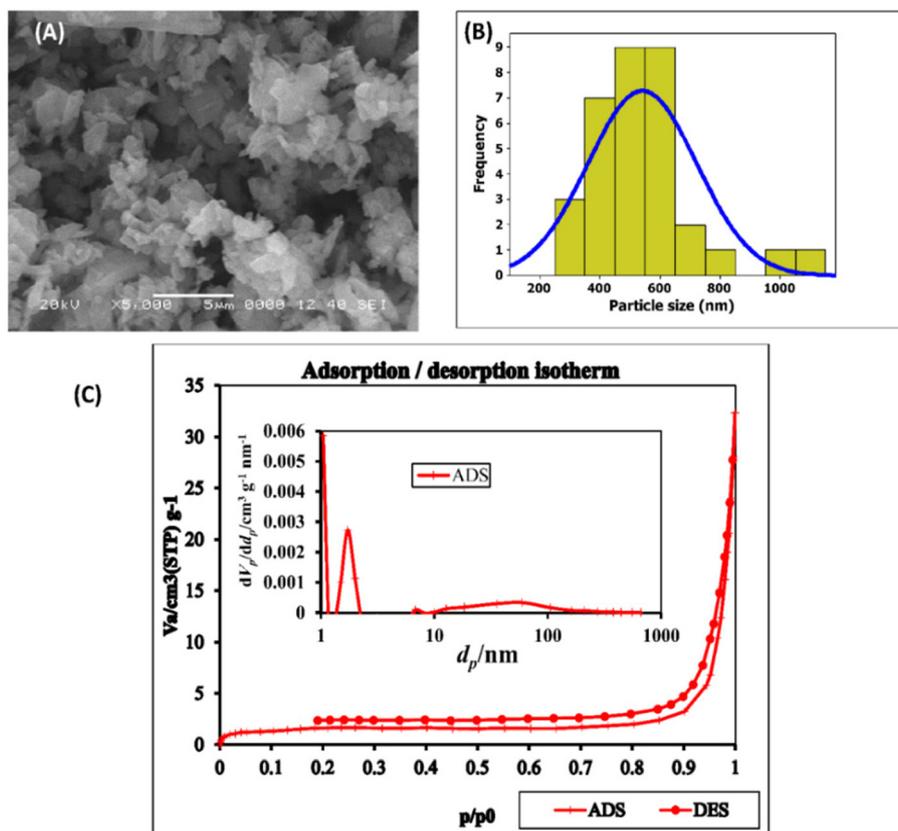
Fig. 1 (A) SEM image of the synthesised MIL-101(Fe)MOF, (B) the size of nanoparticles, and (C) N$_2$ adsorption–desorption isotherms, and the inset presenting the pore size distribution curves of MIL-101(Fe)MOF NPs at 77 K.

600 nm. The porous structure of the MIL-101(Fe)MOF NPs and its BET surface area were determined using nitrogen adsorption–desorption at 77 K, as shown in Fig. 1C. The MIL-101(Fe) MOF NPs exhibited a BET surface area of 125.49 m^2 g^{-1}. The framework exhibited a mean pore diameter of 25.04 nm and a total pore volume of 0.03 cm^3 g^{-1}. This finding is consistent with the information presented in the literature.[34] According to the International Union of Pure and Applied Chemistry (IUPAC), the synthesized MIL-101(Fe)MOF NP material is a compound with mesoporous properties, where a mesoporous material is defined as having pores with diameters ranging from 2 to 50 nm.[35] The adsorption isotherm of MIL-101 follows a type I pattern, which is consistent with previous findings.

FTIR and XRD analyses of MIL-101(Fe)MOF NPs before and after loading

To confirm the conjugation of folic acid onto MIL-101(Fe)MOF NPs, as well as the effective loading of DO8, Fourier-transform infrared spectroscopy (FTIR) was conducted to analyze the functional groups present in MIL-101(Fe)MOF NPs, MIL-101 (Fe)MOF-FA NPs, and MIL-101(Fe)MOF-FA@DO8 NPs (Fig. 2A). MIL-101(Fe)MOF NPs exhibit characteristic peaks at 532, 736.72, 1362.81, and 1625.23 cm^{-1}. The peak at 532 cm^{-1} represents the chelating bond of Fe^{3+}, while the peak at

736.72 cm^{-1} is attributed to the C=C bond and carboxylic group of terephthalic acid.[36] The absorption peaks at 1541.24 cm^{-1} and 1389.60 cm^{-1} correspond to the symmetric and asymmetric stretching vibrations of the organic ligand O–C=O and the C=C bond of the benzene ring vibration, respectively.[37] The broad peak at 3450 cm^{-1} is attributed to the –OH group of water molecules.[38] The spectra of MIL-101(Fe) MOF-FA reveal a broader and stronger peak at 1650 cm^{-1}, which confirms the conjugation between the terminal amino group of folic acid and the carboxylic group of the organic linker (terephthalic acid) through an amide bond, and this result is consistent with prior research findings.[20] The MIL-101(Fe)MOF-FA@DO8 NP spectrum showed two new peaks, one at 1250 cm^{-1} and one at 1100 cm^{-1}. The 1250 cm^{-1} peak was attributed to an asymmetric C–O–C bond, and the 1040 cm^{-1} peak was related to a symmetrical stretch.[39] Otherwise, the C=C stretch causes a vibration at 1500 cm^{-1}.[40]

The XRD patterns of the prepared materials are shown in Fig. 2B. The clear diffraction peaks correspond to MIL-101(Fe) MOF NPs (2θ = 9.42, 9.66, and 18.88). This indicates that MIL-101(Fe)MOF NPs were successfully synthesized. In addition, the X-ray powder patterns displayed are consistent with the MIL-101(Fe)MOF NPs samples documented in the literature.[41,42] In MIL-101(Fe)-FA NPs, on the other hand, the diffraction peak is not nearly as strong as it is in MIL-101(Fe)
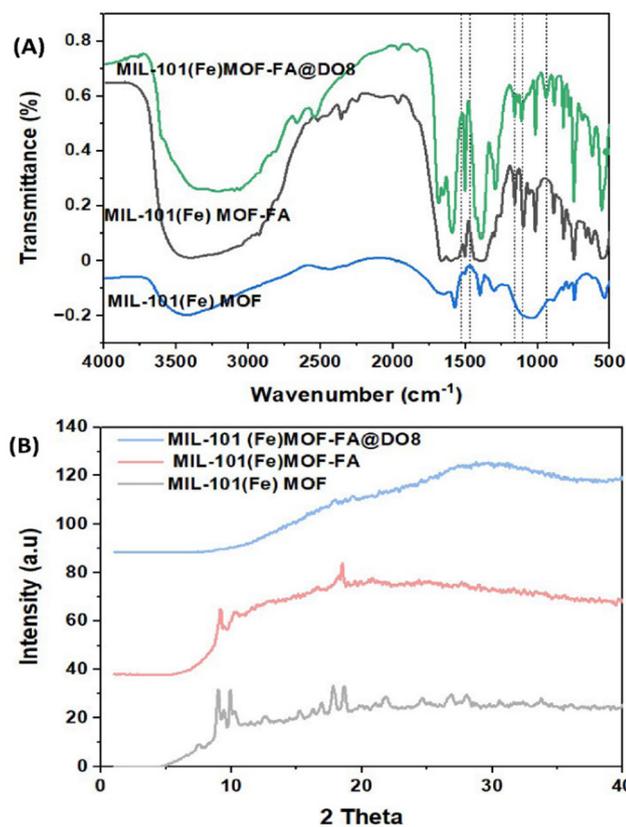
Fig. 2 (A) FTIR and (B) XRD analyses of the synthesized MIL-101(Fe) MOF NPs, MIL-101(Fe)MOF-FA, and MIL-101(Fe)MOF-FA@DO8.

Fig. 3 (A) The UV absorption of the synthesized MIL-101(Fe)MOF NPs, MIL-101(Fe)MOF-FA NPs, and MIL-101-FA@DO8 NPs. (B) PL intensity for the synthesized NPs. The inset photograph of DO8 and MIL-101(Fe) MOF-FA@DO8 under a UV lamp with a wavelength of 356 nm.

MOF, and the crystallinity of the two is very different. The MIL-101(Fe)MOF-FA@DO8 NP material has broad and low-intensity diffraction peaks.

Photochemical analysis of MIL-101(Fe)MOF NPs before and after loading

The UV absorption spectra of MIL-101(Fe)MOF nanoparticles, MIL-101(Fe)MOF-FA nanoparticles, and MIL-101(Fe) MOF-FA@DO8 nanoparticles were examined to confirm the encapsulation of the photosensitizer DO8 within the MIL-101 (Fe)MOF-FA framework (Fig. 3A). Fig. 3A illustrates that DO8 exhibits two separate absorption peaks at wavelengths of 273 nm and 372 nm. Upon loading DO8 into MIL-101(Fe) MOF-FA nanoparticles, a faint absorption peak appears near 400 nm for MIL-101(Fe)MOF-FA@DO8 nanoparticles, signifying the successful incorporation of DO8 into the MOF framework. Furthermore, the encapsulation of DO8 results in a significant reduction of the emission peak at around 450 nm (Fig. 3B), reinforcing the assertion that DO8 has been effectively integrated into the MIL-101(Fe)MOF-FA nanoparticles. This reduction in emission is similar to observations when chemotherapeutic agents like Doxorubicin are encapsulated in other carriers such as tetraphenylethylene, where the blue light emitted by the carrier is also quenched.[43] This suggests that encapsulation within the MOF structure affects the fluorescence characteristics of the loaded substance.
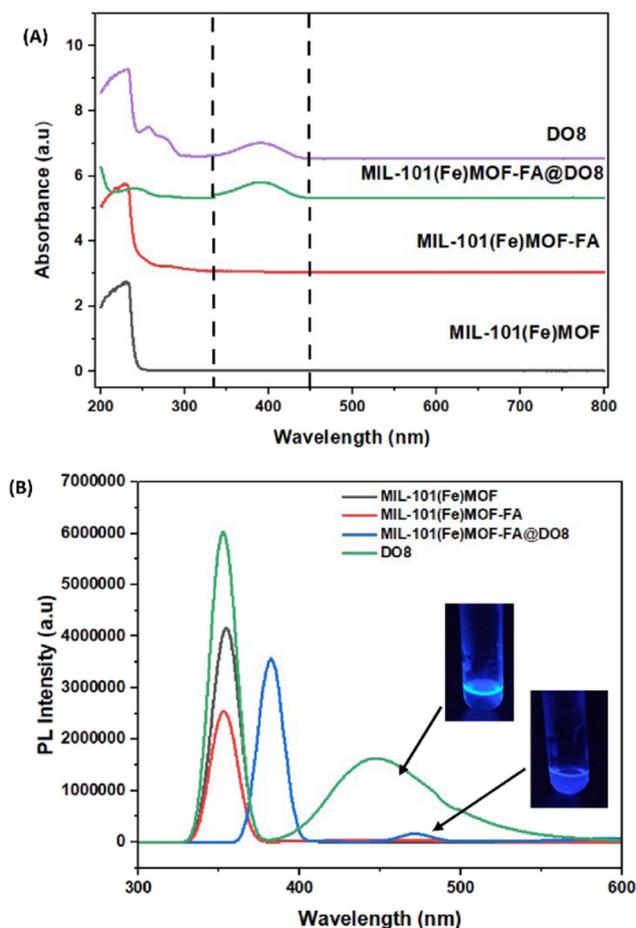
The stability of MIL-101(Fe)MOF-FA@DO8 NPs in solution was assessed over 21 days at 37 °C and pH 7 (physiological conditions) using UV-Vis spectroscopy (Fig. S3†). Minimal changes in the longitudinal band position and intensity indicated good optical stability. Critically, insignificant agglomeration was observed after 21 days, suggesting that the NPs maintain their dispersibility and structural integrity, crucial for effective drug delivery and long-term storage/administration. A key finding was the insignificant agglomeration of the nanoparticles after 21 days, a crucial requirement for clinical translation. This indicates that MIL-101(Fe)MOF-FA@DO8 NPs maintain excellent dispersibility and stability over time, which is essential for maximizing drug delivery and therapeutic efficacy. This stability is particularly important for long-term storage and use within biological systems.[44] In addition to UV-Vis analysis, FTIR spectroscopy confirmed the stability of the nanoparticles under physiological pH conditions. The FTIR spectra of the MIL-101(Fe)MOF-FA@DO8 NPs revealed no significant alterations in their characteristic functional groups or overall chemical structure, further supporting their chemical stability throughout the study period.

DLS characterization of MIL-101(Fe)MOF NPs before and after loading

Particle size is a crucial factor in drug delivery applications, as it has a significant impact on the release of the enclosed drug. MOFs are crystalline materials with pores, and the size of their particles is determined by the solvent and preparation method used. MOFs are synthesized using a solvent system made up of water and methanol, resulting in larger particle sizes. Conversely, using DMF as the solvent leads to smaller particle sizes because the cross-linker in DMF is more soluble than in water and methanol. The synthesized MIL-101(Fe)MOF NPs had a particle size of 393 ± 18.42 nm and a PDI of 0.583 ± 0.17 in the case of dispersion in water and this result aligns with the particle size calculated using SEM. However, MIL-101(Fe)MOF-FA NPs got bigger in size after folic acid was added to the surface and DO8 was enclosed. Their sizes went up to 458 ± 11.95 nm and 773.6 ± 15.43 nm, respectively. The PDI values are 0.549 ± 0.34 and 0.619 ± 0.15, respectively. The synthesized MOFs displayed a positive zeta potential under neutral conditions, as their isoelectric points (IEPs) were all above 7.[36] The MIL-101(Fe)MOF particles exhibited negative zeta potential values after being conjugated with folic acid and loaded with DO8, indicating successful encapsulation. Table 1 provides specific results of DLS and PDI as well as the loading efficiency of MIL-101(Fe)MOF-FA@DO8 (30%) and MIL-101(Fe)MOF-FA@DO8 (50%) NPs based on the standard curve of DO8 (Fig. S4†).
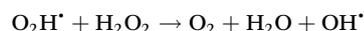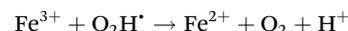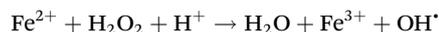
ROS generation profile

Singlet oxygen measurements. As is well known, photosensitized singlet oxygen generation requires oxygen, light of an appropriate wavelength, and a photosensitizer. Upon light absorption, the photosensitizer transitions to its singlet excited state, and then to its triplet state *via* intersystem crossing. This longer-lived triplet state transfers energy to the triplet oxygen, producing singlet oxygen (Fig. S5†).[45] Φ_Δ was measured by detecting singlet oxygen phosphorescence at ~1275 nm in acetonitrile, following a modified McKenzie method.[46] The quantum yield of singlet oxygen generation (Φ_Δ) was determined by comparing the initial emission intensity of the compounds with that of the standard, tris(bipyridine)ruthenium(II) chloride (Φ_Δ = 57% in acetonitrile; Fig. S5†).[46] The synthesized DO8 exhibited a Φ_Δ value of 0.27.[46] Incorporation of DO8 into the MIL-101(Fe)MOF-FA@DO8 nanoparticle increased Φ_Δ to 0.35. This enhancement facilitates singlet oxygen production and, upon targeted laser activation,

promotes the release of both $^1O_2$ and $^\cdot OH$ into tumor tissue *via* a Fenton-like reaction. This dual ROS generation mechanism synergistically induces oxidative damage and tumor cell death, like the TCPP-MIL-101(Fe) conjugate reported by Chen *et al*.[47]

Detection of peroxidase (POD) like activity of MIL-101(Fe) MOF-FA@DO8 using methylene blue and hydrogen peroxide

Fig. 4A and B illustrate the photodegradation process of methylene blue (MB) in the presence of hydrogen peroxide (H_2O_2), facilitated by the generation of reactive oxygen species (ROS) from MIL-101(Fe)MOF-FA@DO8 under light irradiation (400 nm, 1.5 W cm^{-2}). The ongoing irradiation results in a gradual decrease in the UV–vis absorption spectrum of MB at a wavelength of 664 nm. The shift of the absorption band to a lower intensity over time indicates MB degradation, attributed to hydroxyl radical ($^\cdot OH$) generation. The degradation of MB *via* ROS generation indicates the presence of highly reactive species in the solution, which is directly associated with the photocatalytic process.[48] The significance of MIL-101(Fe) MOF-FA@DO8 NPs in this process is notable. MIL-101(Fe)MOF NPs are an iron(III)-based metal–organic framework (MOF) recognized for its superior characteristics in drug delivery and catalysis, attributed to its capacity to produce reactive oxygen species upon exposure to light and hydrogen peroxide. The reaction mechanism described involves the coordination separation of iron(III) in the presence of H_2O_2, a characteristic observed in tumor environments,[49] as illustrated by the following reactions:

$$Fe^{2+} + H_2O_2 + H^+ \rightarrow H_2O + Fe^{3+} + OH^\cdot$$

$$Fe^{3+} + H_2O_2 \rightarrow Fe^{2+} + O_2H^\cdot + H^+$$

$$Fe^{3+} + O_2H^\cdot \rightarrow Fe^{2+} + O_2 + H^+$$

$$O_2H^\cdot + H_2O_2 \rightarrow O_2 + H_2O + OH^\cdot$$

The efficient generation of ROS from the MIL-101(Fe)MOF upon exposure to light and H_2O_2 highlights its potential for targeted photodegradation in environments like tumors, where the concentration of H_2O_2 is typically elevated.

In vitro drug release and kinetic performance in a stimulated tumor environment

Drug release efficiency is a crucial measure for assessing the effectiveness of a drug carrier. Under normal physiological conditions, the normal tissue cell cytosol has a pH of 7.2 to

Table 1 DLS characterization and drug loading of DO8 on MIL-101-FA

Formulation	DLS results			Drug loading	
	Particle size (nm)	PDI	Zeta potential (mV)	Drug loading efficiency (%) ± SD	Drug loading capacity ± SD (mg)/g
MIL-101(Fe) MOF NPs	393 ± 18.42	0.583 ± 0.17	6	—	—
MIL-101-FA NPs	458 ± 11.95	0.549 ± 0.34	−25	—	—
MIL-101-FA@30%DO8 NPs	773.6 ± 15.43	0.619 ± 0.15	−26.5	75.05 ± 2.3	225.18 ± 1.42
MIL-101-FA@50%DO8 NPs				84.98 ± 1.76	424.9 ± 2.97
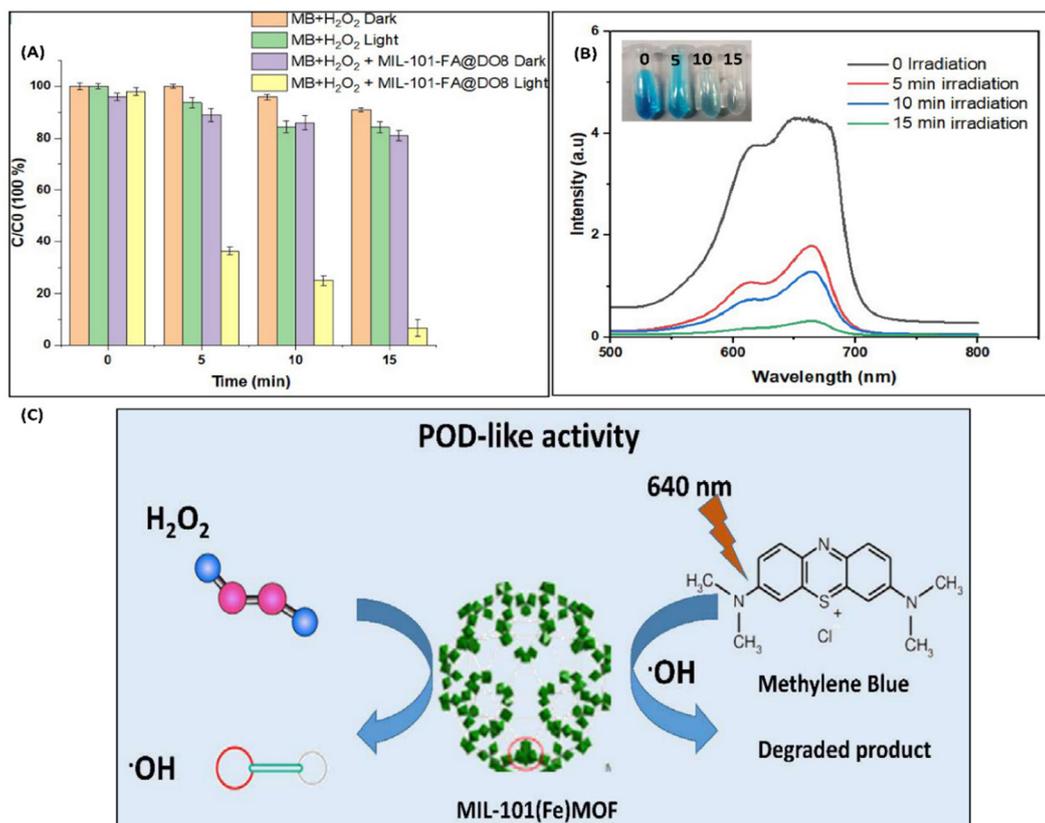
Fig. 4 (A and B) illustrates the degradation of methylene blue (MB) by hydroxyl radicals (˙OH) using MIL-101(Fe)MOF solution under 400 nm LED light irradiation (1.5 W cm^{-2}). The insets show photographic images that visually depict the reduction of the blue color of the MB solution, indicating its degradation. (C) A proposed mechanism is presented for the peroxidase-like (POD-like) activity of the MIL-101(Fe)MOF.

7.4, whereas tumor tissue has a pH of approximately 5.[50] To test how pH affects the release of DO8 from the MIL-101(Fe) MOF-FA@50% DO8 NPs that were made, we looked at the total release of DO8 in both a normal physiological environment and a tumor microenvironment. Fig. 5 demonstrates that the nanoplatform exhibits gradual release in PBS buffers of varying pH levels, followed by steady stabilization over a period of 72 hours. The release rate at pH 5 is found to be 82.02%, but at pH 7.4, it is approximately 51%. The MIL-101(Fe) MOF-FA@DO8 NP structure undergoes loosening in a weakly acidic environment as a result of deformation effects in an acidic medium.[51] This loosening enables DO8 to be released from the nanoplatform. Conversely, when exposed to a mildly basic environment, the nanoplatform's structure is compact, which hinders DO8 release. Other studies show similar behavior. The ZIF-8 structure collapsed, causing the AuNCs and DOX to be released more quickly in the tumor cells. This process resulted in improved performance of PDT/chemotherapy in the pH-responsive AuNCs@MOF-DOX nanoplatform. The rate of DOX release exhibited an increase to 77.1% when the pH value reached 5.5.[47]

However, Meng and colleagues developed a multifunctional Ce6@RMOF nanocarrier that exhibited sensitivity to low pH and demonstrated increased release of Ce6 at pH 5.0 com-
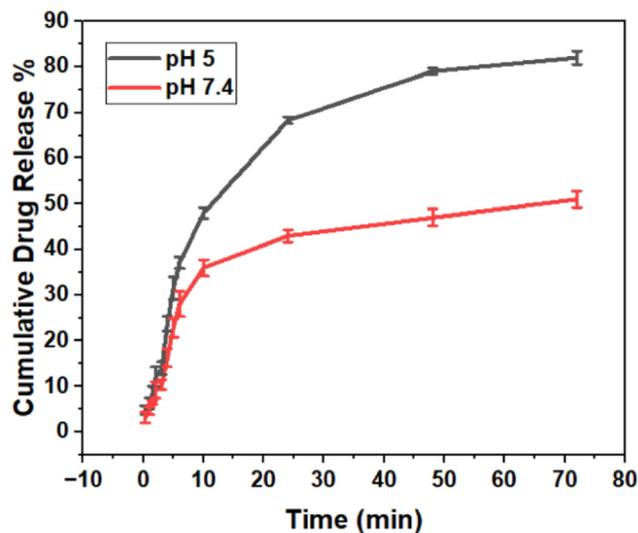
Fig. 5 The drug release profile of MIL-101-FA@50% DO8 at pH = 5 and pH = 7.4.

pared to pH 7.4.[52] In addition, the Ir@MOF/P NPs demonstrated a higher rate of Ir(III) complex release at pH 5.4 (35.1%) compared to pH 7.4 (2.26%) by the third day.[53] The release

Table 2 Mathematical models (zero order, first order, Higuchi, and Korsmeyer–Peppas) and different kinetics parameters of DO8 release from MIL-101-FA@50% DO8 at pH 5

Kinetic model	Fitting equation	R^2	K
Zero order	$Q_t = Q_0 + K_0 t$ $y = 0.6044x + 0.9341$	0.9287	0.6044
First order	$\text{Log } Q_t = \log Q_0 - Kt/2.303$ $y = 0.2626 \ln(x) + 0.9319$	0.9282	3.08
Higuchi	$Q = K_H t^{1/2}$ $y = 10.976x + 1.5991$	0.9173	10.976
Korsmeyer–Peppas	$M_T/M_\infty = Kt^n$ $y = 0.5796x - 0.0094$	0.9779	$K = 0.978588$ $n = 0.5796$

kinetics of DO8 were analyzed by fitting the time profiles of DO8 release from the MIL-101 MOF nanocarrier into various kinetics models (Fig. S4†). The kinetic models for drug release consist of the zero-order, first-order, Higuchi, and Korsmeyer–Peppas models. The outcomes that correlate with K and R, which represent the constant rate and correlation coefficient, respectively, are depicted in Fig. S6† and Table 2. The Korsmeyer–Peppas model had a better fit for all data points, evident from its higher R^2 value in comparison to other coefficients. The diffusion exponent (n) values at pH 5 and 7.4 were 0.5796, 0.490, and greater than 0.45, showing non-Fickian transport.[54]

### In vitro anticancer effects of the synthetic compounds

The synthesized compounds were assessed for their cytotoxicity on the viability of normal human lung fibroblast (Wi-38), breast carcinoma (MDA), hepatoma (HepG-2), and lung carcinoma (A549) cell lines. The evaluation was conducted at various concentrations, ranging up to 800 μg mL^{-1} for each compound in the absence and presence of light. The evaluated compounds exhibited distinct impact profiles on the cellular proliferation of all examined cell lines, encompassing both normal and cancerous cells. Overall, the synthesized compounds demonstrated minimal toxicity towards normal human Wi-38 cells and demonstrated a moderate toxic effect on MDA and A549 cells, while demonstrating significant toxicity towards HepG-2 cells in a dose-dependent manner under dark conditions (Fig. 6A). Notably, HepG-2 cells exhibited the highest sensitivity to the synthetic compounds, as indicated by the lowest IC$_{50}$ values and the highest selectivity index (SI) values, regardless of whether the cells were exposed to darkness or light. This information is presented in Tables 3 and 4. The IC$_{50}$ values of the synthesized compounds (MIL-101-FA@50% DO8, MIL-101-FA@30% DO8, MIL-101(Fe)MOF, MIL-101(Fe)MOF-FA, and DO8) were determined to be 125.1, 151.3, 212.3, 134.5, and 94.59 μg mL^{-1}, respectively, when tested against MDA cells under dark conditions. The corresponding selectivity index (SI) values for MIL-101(Fe) MOF-FA@50% DO8, MIL-101(Fe)MOF-FA@30% DO8, MIL-101 (Fe)MOF, MIL-101(Fe)MOF-FA, and DO8 were 3.27, 2.84, 2.08, 3.02, and 2.79, respectively. The IC$_{50}$ values of the synthetic compounds against HepG-2 cells were found to be 88.67, 105.9, 222.2, 117.6, and 69.67 μg mL^{-1}, with corresponding SI

values of 4.26, 4.06, 1.99, 3.46, and 3.79, respectively (Table 3). Additionally, the IC$_{50}$ values of the synthetic compounds against A549 cells were found to be 132.4, 149.5, 290.3, 181.2, and 78.19 μg mL^{-1}, with corresponding SI values of 3.09, 2.87, 1.52, 2.24, and 3.39, respectively (Table 3). Nevertheless, cytotoxicity studies revealed that, under the same experimental conditions, the synthetic compounds, except for MIL-101(Fe) MOF and MIL-101(Fe)MOF-FA, exhibited significantly higher inhibitory activity in HepG-2 cells compared to MDA and A549 cells under dark conditions.

However, compound MIL-101(Fe)MOF-FA@50% DO8 demonstrated greater selectivity against HepG-2 and MDA cells in the presence of light, compared to compound MIL-101(Fe) MOF-FA@30% DO8 and compound DO8. HepG2 tumor cells exhibit the highest level of sensitivity among cancer cells when treated with synthetic compounds in the presence of light. In addition, the ability to inhibit cell proliferation in a dose-dependent manner is demonstrated by synthetic compounds.[55] This inhibition refers to the concentration of the compounds needed to reduce cell activity under both dark and light conditions (Fig. 6A and B, respectively).

Table 4 presents the IC$_{50}$ values of various compounds under specific lighting conditions. The most potent antitumor activity against HepG-2 cells was observed with DO8 (IC$_{50}$ = 3.98 μg mL^{-1}), followed by MIL-101(Fe)MOF-FA@50% DO8 (IC$_{50}$ = 8.94 μg mL^{-1}) and MIL-101(Fe)MOF-FA@30% DO8 (IC$_{50}$ = 11.78 μg mL^{-1}). Furthermore, MIL-101(Fe) MOF-FA@50% DO8 demonstrated the highest phototoxicity against HepG-2 cells (IC$_{50}$ = 8.94 μg mL^{-1}), which are known to overexpress the folate receptor. This phototoxicity was significantly lower in MDA cells (IC$_{50}$ = 12.48 μg mL^{-1}), which express the folate receptor moderately, and drastically reduced in A549 cells (IC$_{50}$ = 47.82 μg mL^{-1}), which lack the receptor.[56,57] The higher phototoxicity of MIL-101(Fe) MOF-FA@50% DO8 in HepG-2 cells likely stems from its folate receptor targeting, demonstrating specificity for folate-receptor overexpressing cells and suggesting potential for targeted tumor therapy.

This finding demonstrates that DO8 exhibits considerable cytotoxicity even in the absence of light (dark conditions), as evidenced by the IC$_{50}$ values presented in Table 3. Specifically, the IC$_{50}$ values for DO8 were determined to be 69.67 μg mL^{-1} for HepG-2 cells, 94.59 μg mL^{-1} for MDA cells, and 78.19 μg
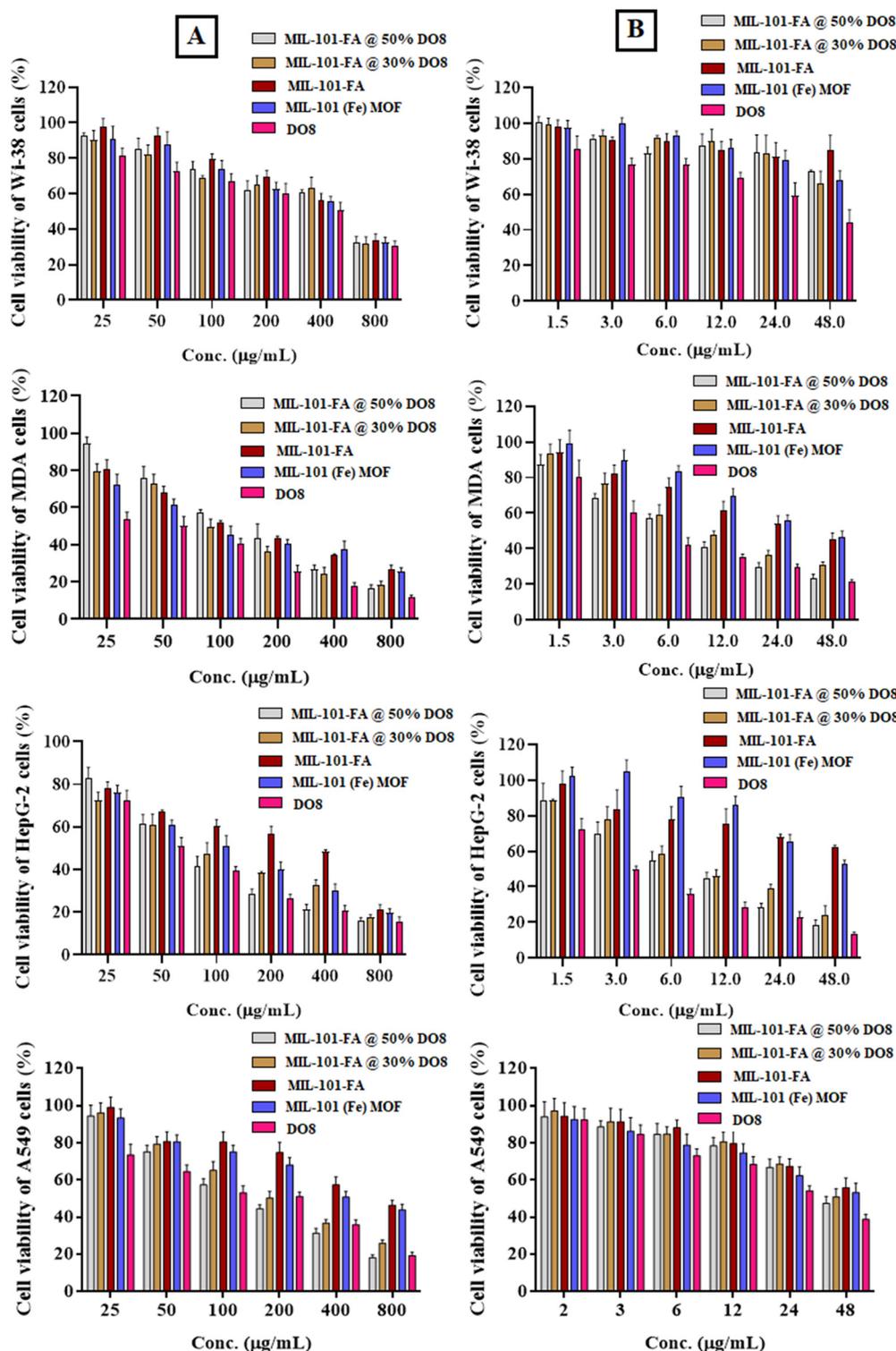
Fig. 6 Effect of the synthesized compounds (MIL-101-(Fe) MOF-FA@50% DO8, MIL-101 (Fe)-MOF-FA@30% DO8, MIL-101 (Fe) MOF-FA, MIL-101(Fe) MOF and DO8) on the cell viability of normal human lung fibroblast (W-38), breast cancer (MDA), hepatoma (HepG-2), and lung cancer (A549) cell lines at various concentrations (0 to 800 μg ml^{-1}) under dark conditions (A) and at concentrations of 1.5, 3.0, 6.0, 12.0, 24.0 and 48.0 μg ml^{-1} under light conditions (B) after treatment for 48 h compared to untreated cells (expressed as triplicate values of mean ± SD).

Table 3 The antitumor activity of the prepared derivatives under dark conditions against HepG-2, MDA-MB-231 and A549 cells compared with normal human cells (Wi-38) expressed in IC_{50} (µg mL^{-1}) and SI values

Sample code	Wi-38 IC_{50}	HepG-2		MDA-MB-231		A549	
		IC_{50}	SI	IC_{50}	SI	IC_{50}	SI
MIL-101 (Fe) MOF-FA@50% DO8	409.7 ± 25.68	88.67 ± 6.23	4.26 ± 0.29	125.1 ± 3.78	3.27 ± 0.21	132.4 ± 6.59	3.09 ± 0.19
MIL-101 (Fe) MOF-FA@30% DO8	429.8 ± 26.18	105.9 ± 5.04	4.06 ± 0.25	151.3 ± 3.98	2.84 ± 0.17	149.5 ± 5.98	2.87 ± 0.17
MIL-101 (Fe) MOF-FA	442.3 ± 28.03	222.2 ± 7.39	1.99 ± 0.13	212.3 ± 6.03	2.08 ± 0.13	290.3 ± 7.56	1.52 ± 0.09
MIL-101(Fe) MOF	406.5 ± 19.77	117.6 ± 5.28	3.46 ± 0.17	134.5 ± 6.57	3.02 ± 0.15	181.2 ± 5.67	2.24 ± 0.11
DO8	264.7 ± 22.91	69.67 ± 5.85	3.79 ± 0.33	94.59 ± 4.84	2.79 ± 0.24	78.19 ± 2.82	3.39 ± 0.29

Table 4 The antitumor activity of the prepared derivatives under light conditions against HepG-2, MDA-MB-231, and A549 cells compared with normal human cells (Wi-38) expressed in IC_{50} (µg mL^{-1}) and SI values

| Sample code	Wi-38 IC_{50}	HepG-2		MDA-MB-231		A549	
		IC_{50}	SI	IC_{50}	SI	IC_{50}	SI
MIL-101 (Fe) MOF-FA@50% DO8	84.15 ± 9.76	8.94 ± 0.83	9.41 ± 1.09	12.48 ± 1.08	6.74 ± 0.78	47.82 ± 2.75	1.76 ± 0.16
MIL-101 (Fe) MOF-FA@30% DO8	97.05 ± 5.49	11.78 ± 1.09	8.24 ± 0.47	15.63 ± 1.24	6.21 ± 0.35	53.34 ± 3.89	1.82 ± 0.11
MIL-101 (Fe) MOF-FA	104.8 ± 12.01	53.86 ± 2.43	1.95 ± 0.22	76.94 ± 3.67	1.36 ± 0.16	83.07 ± 6.19	1.66 ± 0.19
MIL-101(Fe) MOF	98.73 ± 3.82	58.54 ± 3.17	1.69 ± 0.07	78.84 ± 2.73	1.25 ± 0.05	57.29 ± 3.31	1.72 ± 0.27
DO8	28.02 ± 2.45	3.98 ± 0.26	7.04 ± 0.62	6.82 ± 0.71	4.11 ± 0.36	15.11 ± 2.06	1.85 ± 0.12

mL^{-1} for A549 cells. These results suggest that DO8 exhibits inherent anticancer activity, independent of light activation, and thus holds potential as a chemotherapeutic agent. However, a significant increase in cytotoxicity was observed upon exposure to a 400 nm laser for 10 minutes. Cell viability decreased dramatically, reaching 16% for HepG-2 cells, 21% for MDA cells, and 15.11% for A549 cells (Table 4). This substantial reduction in viability underscores the potent phototoxicity of DO8 and likely involves the generation of singlet oxygen upon light exposure. Singlet oxygen is known to induce cellular damage *via* oxidative stress. This dual-action mechanism—exhibiting both chemotherapeutic activity in the dark and photodynamic therapeutic activity under light—positions DO8 as a promising candidate for photochemotherapy.

Incorporating DO8 into the MIL-101(Fe)MOF-FA nanocarrier significantly improved DO8's biocompatibility, as demonstrated by increased Wi-38 normal cell tolerance and survival. Critically, the MOF-FA mitigated DO8's cytotoxicity in these normal cells, effectively widening the therapeutic window and minimizing the risk of off-target toxicity in healthy tissues. This enhanced biocompatibility makes DO8 more promising for clinical applications. Furthermore, the MIL-101(Fe)MOF-FA system facilitated targeted therapy. A549 cells (folic acid receptor-negative) showed low toxicity with the DO8-loaded MOF-FA, both in the dark and under light exposure. This confirms the crucial role of the MOF-FA's folate-targeting in selectively delivering DO8 to folate-receptor-expressing cancer cells, such as HepG-2 and MDA cell lines. This targeted delivery is evidenced by the significantly improved therapeutic outcomes observed in HepG-2 and MDA cells, compared to A549 cells, particularly under light exposure.

It should also be noted that the small size of the MIL-101 (Fe)MOF-FA@DO8 nanoplatform facilitates enhanced cellular penetration, enabling more effective internalization of DO8 and maximizing its cytotoxic effects within target cells.[58] This nano-sized delivery system also increases DO8 concentration within cancer cells and provides a sustained release profile, crucial for efficient chemotherapeutic and photodynamic treatment.[59]

The MTT assay results, corroborated by the photomicrographs in Fig. 7A, strongly indicate the cytotoxic effects of the synthesized compounds on HepG-2 cells. These cells were selected due to their high responsiveness to treatment. After 48 hours of exposure to the compounds at their respective IC_{50} doses, significant structural changes were observed in the treated cells under both dark and light conditions. While untreated HepG-2 cells maintained their normal morphology, the treated cells displayed clear signs of cell destruction. These changes included cell shrinkage, membrane blebbing, and detachment from the culture substrate. Such morphological alterations are characteristic of apoptosis or necrosis, demonstrating the potent cytotoxicity of the compounds.[60] The observed changes highlight the effectiveness of the synthesized compounds in disrupting cellular integrity. Specifically, MIL-101(Fe)MOF-FA at 50% DO8, MIL-101(Fe) MOF-FA at 30% DO8, and DO8 exhibited strong activity in inducing cell death.

This study highlights the crucial role of reactive oxygen species (ROS) in the observed cytotoxic effects. ROS production is a key mechanism of photodynamic therapy (PDT). In PDT, photosensitizers (PSs) like DO8 are activated by light, generating ROS that damage cellular components such as proteins, lipids, and DNA.[61] Our findings demonstrate light-induced
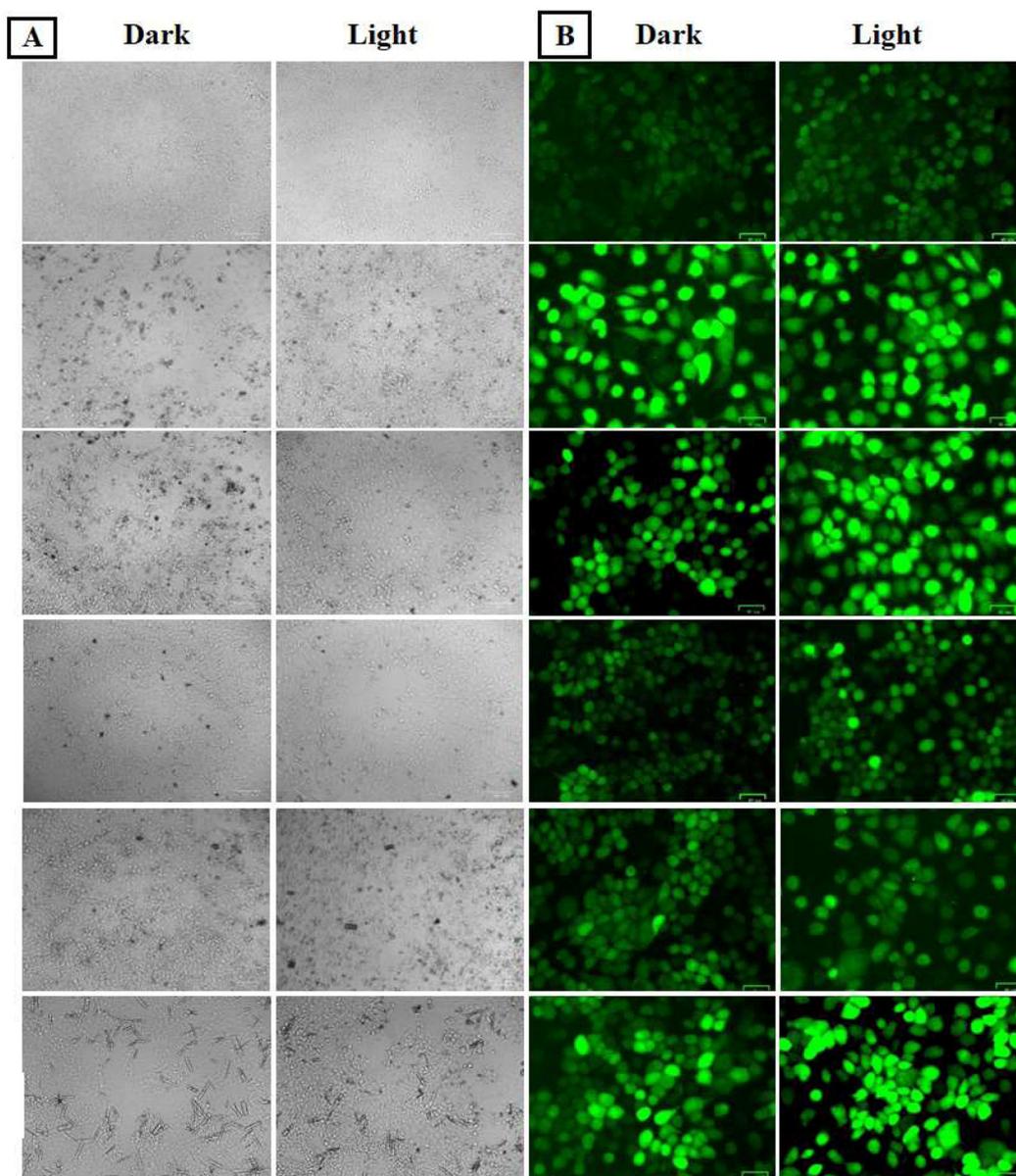
Fig. 7 (A) Bright images of HepG-2 cells incubated with the synthetic compounds showing enhanced intracellular uptake. (B) Fluorescence images of HepG-2 cells showing the ROS formation by the synthetic compounds. Cells were treated with synthetic compounds at IC_{50} doses for 48 h of treatment as compared to control (untreated) cells.

ROS generation with these compounds, indicating their effective function under photodynamic conditions.

Fluorescence microscopy further elucidated ROS production within HepG-2 cells. A clear correlation emerged: increasing the DO8 concentration led to increased ROS levels and a corresponding decrease in cell viability. This confirms the direct relationship between the photosensitizer concentration and ROS generation. Higher DO8 concentrations result in greater ROS production, a critical factor because these ROS, particularly singlet oxygen and free radicals, are highly reactive molecules. They induce oxidative stress, ultimately leading to cellular damage and cell death. These findings are

consistent with prior work showing a relationship between ROS levels, PS concentrations, and light exposure. For example, Malina *et al.* (2016) investigated the formation of reactive oxygen species (ROS) in G361 cells exposed to TMPyP and $ZnTPPS_4$ photosensitizers at varying concentrations and irradiation doses.[62]

Fig. 8A and B demonstrate the apoptosis-mediated antitumor activity of the modified MIL-101-FA@50% DO8 compound in HepG-2 cells, assessed *via* flow cytometry using annexin V/PI staining. Cells were treated with the compound at its IC_{50} dose under both dark and light conditions. Untreated control HepG-2 cells, whether kept under dark or light conditions,
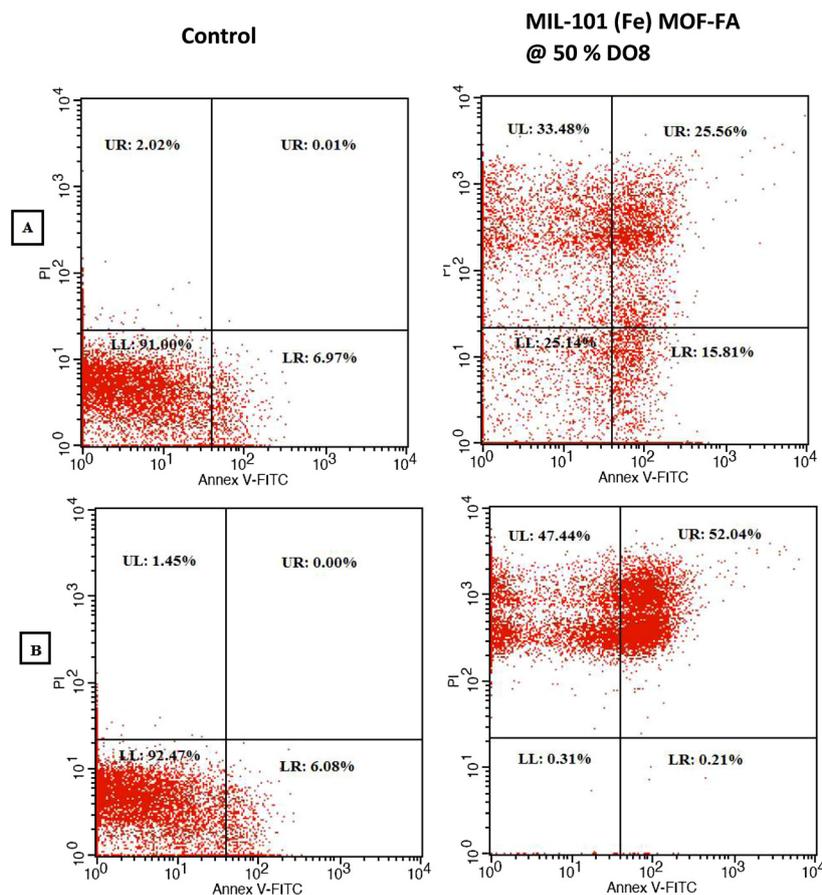
Fig. 8 Verification of apoptotic and necrotic mechanisms of the MIL-101 (Fe) MOF-FA@50%DO8 compound in the treated and untreated (control) HepG-2 cells using flow cytometric analysis of Annexin V/PI-stained under dark (A) and light (B) conditions.

showed minimal cell death, with the living cell population exceeding 90%. Treatment with MIL-101-FA@50% DO8 NPs in the dark resulted in a significant increase in both early apoptotic (15.81%) and late apoptotic (25.56%) populations, alongside a necrotic population of 33.48% (Fig. 8A). Under light conditions, the treatment led to a substantial increase in late apoptotic cells (52.04%) and a prominent necrotic population (47.44%) as indicated by strong PI staining (Fig. 8B). This heightened necrosis under light conditions may be attributed to increased ROS generation compared to dark conditions, resulting in extensive membrane rupture following treatment with the modified MIL-101-FA@50% DO8 compound.

Mechanism of cell death

Untreated HepG-2 cells showed minimal Annexin V/PI staining (10%). However, treatment with MIL-101 (Fe) MOF-FA@50% DO8 in the dark significantly increased early apoptosis (15.81%), late apoptosis (25.56%), and necrosis (33.48%). This indicates that even in the dark, MIL-101 (Fe) MOF-FA@50% DO8 induces oxidative stress and membrane damage, albeit less than in light. It is most likely that DO8 contributes to cytotoxicity through chemotherapy-induced apoptosis and necrosis *via* ROS production.

Upon light exposure, the MIL-101 (Fe) MOF-FA@50% DO8 compound significantly increases both late apoptosis (52.04%) and necrosis (47.44%). This effect is driven by a substantial increase in the generation of reactive oxygen species (ROS), particularly singlet oxygen, which leads to heightened oxidative damage of cellular membranes. The accumulation of ROS under light exposure induces extensive cell membrane rupture, explaining the larger necrotic population compared to dark conditions. This intense ROS-mediated oxidative stress in the presence of light triggers both early and late apoptosis and further promotes necrosis by causing ROS-induced membrane damage, ultimately leading to rapid plasma membrane breakdown and cell death.

Conclusion

In this study, we successfully synthesized a novel nanocarrier system, MIL-101 (Fe) MOF-FA@DO8, which demonstrated significant potential for enhancing anticancer therapy through a combination of photodynamic therapy (PDT) and chemotherapy. The system efficiently activated the chemotherapeutic drug DO8 upon light exposure, thereby enhancing its antitu-

mor effects and allowing for a reduction in drug dosage. This reduction not only mitigates potential side effects but also maximizes the efficacy of the treatment. The MIL-101(Fe) MOF nanoparticles showed biocompatibility and light stability, with no harmful effects in the absence of light. Importantly, the nanocarriers were stable under normal physiological conditions, yet exhibited rapid release of DO8 under acidic conditions typical of the tumor microenvironment, providing temporal–spatial selectivity when combined with light stimulation.

Furthermore, the folic acid functionalization on the nanoparticle surface enhanced targeting specificity to HepG-2 cells, resulting in improved treatment efficiency compared to MDA cells. This targeted therapy offers a promising strategy for tumor theranostics. The synergistic combination of phototoxicity and chemotherapy ensures a multifaceted approach to cancer cell death, particularly under light exposure, highlighting the dual mechanism of action facilitated by this system.

Data availability

The ESI† is accessible and contains experimental materials and methodologies for the synthesis, production, and characterization of the photosensitizers, as well as *in vitro* drug release kinetics.

The data that support the findings of this study will be available within the article.

The data are not publicly available before the acceptance of this study for publication.

Conflicts of interest

The authors declare no conflicts of interest.

References

1 F. Akhtar, L. Misba and A. Khan, The dual role of photodynamic therapy to treat cancer and microbial infection, *Drug Discovery Today*, 2024, 104099.

2 J. Dai, L. Fang, Z. Fan, X. Wang, J. Hua, H. Dong, Y. Tu, S. Li, K. He and J. Fang, Triphenylamine-Substituted Nile Red Derivatives with Efficient Reactive Oxygen Species Generation for Robust and Broad-Spectrum Antimicrobial Photodynamic Therapy and Abscess Wound Healing, *Adv. Funct. Mater.*, 2025, 2421072.

3 B. Lv, Y. Zhao, Y. Liang and J. Cao, Extracellular vesicles: an advanced delivery platform for photosensitizers in tumor photodynamic therapy, *Chem. Eng. J.*, 2024, 155438.

4 L. Chen, S. Yan, W.-J. Guo, L. Qiao, X. Zhan, B. Liu and H.-Q. Peng, Boosting type-I ROS production of molecular photosensitizers using bridge-assisted superexchange coupling, *Chem. Sci.*, 2024, 15, 16059–16068.

5 S. Sadiq, S. Khan, I. Khan, A. Khan, M. Humayun, P. Wu, M. Usman, A. Khan, A. F. Alanazi and M. J. H. Bououdina, A critical review on metal-organic frameworks (MOFs) based nanomaterials for biomedical applications: Designing, recent trends, challenges, and prospects, *Heliyon*, 2024, 10, 25521.

6 B. Saboorizadeh, R. Zare-Dorabei, M. Safavi and V. Safarifard, Applications of metal-Organic frameworks (MOFs) in drug delivery, Biosensing, and therapy: a Comprehensive Review, *Langmuir*, 2024, 40, 22477–22503.

7 N. Naz, M. H. Manzoor, S. M. G. Naqvi, U. Ehsan, M. Aslam and F. Verpoort, Porous organic polymers; an emerging material applied in energy, environmental and biomedical applications, *Appl. Mater. Today*, 2024, 38, 102198.

8 G. N. Luncena, C. C. Dod Santos, G. C. Pinto, B. E. Amantea, R. D. Piazza, M. J. Junior and R. F. C. Marques, Surface engineering of magnetic nanoparticles for hyperthermia and drug delivery, *Med. Devices Sens.*, 2020, 3(6), e10100.

9 A. Magadla, Hybrid Nanoplatforms Based on Photosensitizers and Metal/Covalent Organic Frameworks for Improved Cancer Synergistic Treatment Nano-Delivery Systems, *Molecules*, 2025, 30, 884.

10 W. Xu, G. Guan, R. Yue, Z. Dong, L. Lei, H. Kang and G. Song, Chemical Design of Magnetic Nanomaterials for Imaging and Ferroptosis-Based Cancer Therapy, *Chem. Rev.*, 2025, 125(4), 1897–1961.

11 Y. Liu, Y. Jiang, M. Zhang, Z. Tang, M. He and W. Bu, Modulating hypoxia via nanomaterials chemistry for efficient treatment of solid tumors, *Acc. Chem. Res.*, 2018, 51, 2502–2511.

12 T. Ahmad, A. Iqbal, S. A. Halim, J. Uddin, A. Khan, S. El Deeb and A. Al-Harrasi, Recent advances in electrochemical sensing of hydrogen peroxide (H_2O_2) released from cancer cells, *Nanomaterials*, 2022, 12, 1475.

13 K. Jomova, S. Y. Alomar, S. H. Alwasel, E. Nepovimova, K. Kuca and M. Valko, Several lines of antioxidant defense against oxidative stress: Antioxidant enzymes, nanomaterials with multiple enzyme-mimicking activities, and low-molecular-weight antioxidants, *Arch. Toxicol.*, 2024, 98, 1323–1367.

14 Y. Yang and X. Dai, Current status of controlled onco-therapies based on metal organic frameworks, *RSC Adv.*, 2024, 14, 12817–12828.

15 J. Jiang, H. Wang and K. Wang, *Phthalocyanine-Based Functional Polymeric Materials: Design, Synthesis, and Applications*, John Wiley & Sons, 2025.

16 T. Luo, G. T. Nash, Z. Xu, X. Jiang, J. Liu and W. Lin, Nanoscale metal–organic framework confines zinc-phthalo-

cyanine photosensitizers for enhanced photodynamic therapy, *J. Am. Chem. Soc.*, 2021, **143**, 13519–13524.

17 Y.-T. Qin, H. Peng, X.-W. He, W.-Y. Li and Y.-K. Zhang, pH-responsive polymer-stabilized ZIF-8 nanocomposites for fluorescence and magnetic resonance dual-modal imaging-guided chemo-/photodynamic combinational cancer therapy, *ACS Appl. Mater. Interfaces*, 2019, **11**, 34268–34281.

18 X. Li, H. Zheng, J. Chen, M. Xu, Y. Bai and T. Liu, MIL-101 (Fe)@ Ag rapid synergistic antimicrobial and biosafety evaluation of nanomaterials, *Molecules*, 2022, **27**, 3497.

19 R. Abazari, F. Ataei, A. Morsali, A. M. Slawin and C. Carpenter-Warren, A luminescent amine-functionalized metal–organic framework conjugated with folic acid as a targeted biocompatible pH-responsive nanocarrier for apoptosis induction in breast cancer cells, *ACS Appl. Mater. Interfaces*, 2019, **11**, 45442–45454.

20 M. Fytory, K. K. Arafa, W. M. El Rouby, A. A. Farghali, M. Abdel-Hafiez and I. M. El-Sherbiny, Dual-ligated metal organic framework as novel multifunctional nanovehicle for targeted drug delivery for hepatic cancer treatment, *Sci. Rep.*, 2021, **11**, 19808.

21 I. Barwal, R. Kumar, S. Kateriya, A. K. Dinda and S. C. Yadav, Targeted delivery system for cancer cells consist of multiple ligands conjugated genetically modified CCMV capsid on doxorubicin GNPs complex, *Sci. Rep.*, 2016, **6**, 37096.

22 H. A. Khatab, S. F. Hammad, E. M. El-Fakharany, A. I. Hashem and E. A. El-Helw, Synthesis and cytotoxicity evaluation of novel 1, 8-acridinedione derivatives bearing phthalimide moiety as potential antitumor agents, *Sci. Rep.*, 2023, **13**, 15093.

23 S. H. El-Moslamy, M. S. Elnouby, A. H. Rezk and E. M. El-Fakharany, Scaling-up strategies for controllable biosynthetic ZnO NPs using cell free-extract of endophytic Streptomyces albus: characterization, statistical optimization, and biomedical activities evaluation, *Sci. Rep.*, 2023, **13**, 3200.

24 I. Kimiz-Gebologlu and S. S. Oncel, Exosomes: large-scale production, isolation, drug loading efficiency, and biodistribution and uptake, *J. Controlled Release*, 2022, **347**, 533–543.

25 A. M. Alazaly, G. J. Clarkson, M. D. Ward and A. A. Abdel-Shafi, Mechanism of oxygen quenching of the excited states of heteroleptic chromium(III) phenanthroline derivatives, *Inorg. Chem.*, 2023, **62**, 16101–16113.

26 R. R. Cheruku, J. Cacaccio, F. A. Durrani, W. A. Tabaczynski, R. Watson, A. Marko, R. Kumar, M. E. El-Khouly, S. Fukuzumi, J. R. Missert, R. Yao, M. Sajjad, D. Chandra, K. Guru and R. P. Pandey, Epidermal growth factor receptor-targeted multifunctional photosensitizers for bladder cancer imaging and photodynamic therapy, *J. Med. Chem.*, 2019, **62**, 2598–2617.

27 B. Tian, S. Liu, C. Yu, S. Liu, S. Dong, L. Feng, N. Hu and P. Yang, A Metal-Free Mesoporous Carbon Dots/Silica Hybrid Type I Photosensitizer with Enzyme-Activity for Synergistic Treatment of Hypoxic Tumor, *Adv. Funct. Mater.*, 2023, **33**, 2300818.

28 M. Khan, H. Liu, P. Sacco, E. Marsich, X. Li, N. Djaker and J. Spadavecchia, DOTAREM (DOTA)–gold-nanoparticles: Design, spectroscopic evaluation to build hybrid contrast agents to applications in nanomedecine, *Int. J. Nanomed.*, 2022, **17**, 4105.

29 A. Jain and S. Jain, In vitro release kinetics model fitting of liposomes: An insight, *Chem. Phys. Lipids*, 2016, **201**, 28–40.

30 A. M. Eldeeb, E. Serag, M. Elmowafy and M. E. El-Khouly, pH-responsive zeolite-A/chitosan nanocarrier for enhanced ibuprofen drug delivery in gastrointestinal systems, *Int. J. Biol. Macromol.*, 2025, **289**, 138879.

31 P. Kumar, A. Nagarajan and P. D. Uchil, *Analysis of cell viability by the MTT assay*, Cold spring harbor protocols, 2018, vol. 2018. DOI: 10.1101/pdb.prot095505.

32 L. K. McKenzie, I. V. Sazanovich, E. Baggaley, M. Bonneau, V. Guerchais, J. G. Williams, J. A. Weinstein and H. E. Bryant, Metal complexes for two-photon photodynamic therapy: a cyclometallated iridium complex induces two-photon photosensitization of cancer cells under near-IR light, *Chem. – Eur. J.*, 2017, **23**, 234–238.

33 J. H. Lee and Y. J. Yeo, Controlled drug release from pharmaceutical nanocarriers, *Chem. Eng. Sci.*, 2015, **125**, 75–84.

34 Y. Liu, P. Lei, X. Liao and C. J. Wang, Nanoscale metal–organic frameworks as smart nanocarriers for cancer therapy, *J. Nanostruct. Chem.*, 2024, **14**, 1–19.

35 O. Lebedev, F. Millange, C. Serre, G. Van Tendeloo and G. J. Férey, First direct imaging of giant pores of the metal–organic framework MIL-101, *Chem. Mater.*, 2005, **17**, 6525–6527.

36 M.-L. Chen, S.-Y. Zhou, Z. Xu, L. Ding and Y.-H. J. M. Cheng, Metal-organic frameworks of MIL-100 (Fe, Cr) and MIL-101 (Cr) for aromatic amines adsorption from aqueous solutions, *Molecules*, 2019, **24**, 3718.

37 X. Ma, X. Ren, X. Guo, C. Fu, Q. Wu, L. Tan, H. Li, W. Zhang, X. Chen and H. Zhong, Multifunctional iron-based Metal–Organic framework as biodegradable nanozyme for microwave enhancing dynamic therapy, *Biomaterials*, 2019, **214**, 119223.

38 X. Wang, J. Xu, D. Yang, C. Sun, Q. Sun, F. He, S. Gai, C. Zhong, C. Li and P. Yang, Fe₃O₄@MIL-100 (Fe)-UCNPs heterojunction photosensitizer: Rational design and application in near infrared light mediated hypoxic tumor therapy, *Chem. Eng. J.*, 2018, **354**, 1141–1152.

39 Y. Wu, Z. Liu, M. F. Bakhtari and J. Luo, Preparation of GO/MIL-101 (Fe, Cu) composite and its adsorption mechanisms for phosphate in aqueous solution, *Environ. Sci. Pollut. Res.*, 2021, **28**, 51391–51403.

40 A. Pangestu, W. W. Lestari, F. R. Wibowo and L. Larasati, Green electro-synthesized MIL-101 (Fe) and its aspirin detoxification performance compared to MOF-808, *J. Inorg. Organomet. Polym. Mater.*, 2022, **32**, 1828–1839.

41 Ş. S. Bayazit, S. T. Danalıoğlu, M. Abdel Salam and Ö. K. Kuyumcu, Preparation of magnetic MIL-101 (Cr) for efficient removal of ciprofloxacin, *Environ. Sci. Pollut. Res.*, 2017, **24**, 25452–25461.

42 Y. Huang, H. Lin and Y. Zhang, Synthesis of MIL-101 (Fe)/SiO₂ composites with improved catalytic activity for reduction of nitroaromatic compounds, *J. Solid State Chem.*, 2020, **283**, 121150.

43 M. S. Ahmad, M. Khalid, M. A. Shaheen, M. N. Tahir, M. U. Khan, A. A. Braga and H. A. Shad, Synthesis and XRD, FT-IR vibrational, UV–vis, and nonlinear optical exploration of novel tetra substituted imidazole derivatives: A synergistic experimental-computational analysis, *J. Phys. Chem. Solids*, 2018, **115**, 265–276.

44 K. Mahajan and S. Bhattacharya, The advancement and obstacles in improving the stability of nanocarriers for precision drug delivery in the field of nanomedicine, *Curr. Top. Med. Chem.*, 2024, **24**, 686–721.

45 C. Yu, T. Canteenwala, M. E. El-Khouly, Y. Araki, K. Pritzker, O. Ito, B. C. Wilson and L. Y. Chiang, Efficiency of singlet oxygen production from self-assembled nanospheres of molecular micelle-like photosensitizers FC₄S, *J. Mater. Chem.*, 2005, **15**, 1857–1864.

46 M. E. El-Khouly, H. A. Khatab, A. A. Abdel-Shafi and S. F. Hammad, Acridinedione-phthalimide conjugates: Intramolecular electron transfer and singlet oxygen generation studies for optical and photodynamic therapy applications, *Photochem. Photobio. Sci.*, 2024, **23**, 1445–1455.

47 J. Chen, Y. Wang, H. Niu, Y. Wang, A. Wu, C. Shu, Y. Zhu, Y. Bian and K. Lin, Metal–organic framework-based nanoagents for effective tumor therapy by dual dynamics-amplified oxidative stress, *ACS Appl. Mater. Interfaces*, 2021, **13**, 45201–45213.

48 C. Dong, W. Fang, Q. Yi and J. Zhang, A comprehensive review on reactive oxygen species (ROS) in advanced oxidation processes (AOPs), *Chemosphere*, 2022, **308**, 136205.

49 S. N. Mbugua, Targeting tumor microenvironment by metal peroxide nanoparticles in cancer therapy, *Bioinorg. Chem. Appl.*, 2022, **2022**, 5041399.

50 R. Pertiwi, R. Oozeerally, D. L. Burnett, T. W. Chamberlain, N. Cherkasov, M. Walker, R. J. Kashtiban, Y. K. Krisnandi, V. Degirmenci and R. I. Walton, Replacement of chromium by non-toxic metals in lewis-acid MOFs: Assessment of stability as glucose conversion catalysts, *Catalysts*, 2019, **9**, 437.

51 M. Virmani, N. U. Deshpande, S. Pathan and M. J. Jayakannan, Self-reporting polysaccharide polymersome for doxorubicin and cisplatin delivery to live cancer cells, *ACS Polym. Au*, 2021, **2**, 181–193.

52 X. Meng, J. Deng, F. Liu, T. Guo, M. Liu, P. Dai, A. Fan, Z. Wang and Y. Zhao, Triggered all-active metal organic framework: ferroptosis machinery contributes to the apoptotic photodynamic antitumor therapy, *Nano Lett.*, 2019, **19**, 7866–7876.

53 D.-Y. Fu, X. Liu, X. Zheng, M. Zhou, W. Wang, G. Su, T. Liu, L. Wang and Z. Xie, Polymer-metal-organic framework hybrids for bioimaging and cancer therapy, *Coord. Chem. Rev.*, 2022, **456**, 214393.

54 B. Berkowitz, A. Cortis, M. Dentz and H. Scher, Modeling non–Fickian transport in geological formations as a continuous time random walk, *Rev. Geophys.*, 2006, **44**, 1–49.

55 Y. Jiao, H. Sun, Y. Jia, Y. Liu, Y. Gao, M. Xian, S. Shuang and C. Dong, Functionalized fluorescent carbon nanoparticles for sensitively targeted of folate-receptor-positive cancer cells, *Microchem. J.*, 2019, **146**, 464–470.

56 A. Basu, P. Upadhyay, A. Ghosh, D. Chattopadhyay and A. Adhikary, Folic-Acid-Adorned PEGylated Graphene Oxide Interferes with the Cell Migration of Triple Negative Breast Cancer Cell Line, MDAMB-231 by Targeting miR-21/PTEN Axis through NFκB, *ACS Biomater. Sci. Eng.*, 2018, **5**, 373–389.

57 H. Samadian, R.L. Merzel, J.M. Dyson, J. Chen, C. Frey, A. K. Jones, M. Vartanian, B. Ward and M.M.B. Holl, Antitumor effect of folate-binding protein: In vitro and in vivo studies, *Mol. Pharm.*, 2022, **19**(3), 843–852.

58 Z. Teng, L.-Y. Meng, J.-K. Yang, Z. He, X.-G. Chen and Y. Liu, Bridging nanoplatform and vaccine delivery, a landscape of strategy to enhance nasal immunity, *J. Controlled Release*, 2022, **351**, 456–475.

59 G. Li, B. Sun, Y. Li, C. Luo, Z. He and J. Sun, Small-molecule prodrug nanoassemblies: an emerging nanoplatform for anticancer drug delivery, *Small*, 2021, **17**, 2101460.

60 S. Rello, J. Stockert, V. Moreno, A. Gamez, M. Pacheco, A. Juarranz, M. Canete and A. Villanueva, Morphological criteria to distinguish cell death induced by apoptotic and necrotic treatments, *Apoptosis*, 2005, **10**, 201–208.

61 Z. Zhou, J. Song, L. Nie and X. Chen, Reactive oxygen species generating systems meeting challenges of photodynamic cancer therapy, *Chem. Soc. Rev.*, 2016, **45**, 6597–6626.

62 L. Žárská, Z. Malá, K. Langová, L. Malina, S. Binder, R. Bajgar, H. Kolářová and P. Therapy, The effect of two porphyrine photosensitizers TMPyP and ZnTPPS₄ for application in photodynamic therapy of cancer cells in vitro, *Photodiagn. Photodyn. Ther.*, 2021, **34**, 102224.